catalysts

MDPI

Article

Morphology and Crystal-Plane Effects of Fe/W-CeO_2 for Selective Catalytic Reduction of NO with NH_3

Feihu Liu [1,†], Zhong Wang [2,*,†], Da Wang [2], Dan Chen [3], Fushan Chen [1,*] and Xuebing Li [2,*]

1 College of Chemistry and Molecular Engineering, Shandong Provincial Key Laboratory of Biochemical Engineering, Qingdao University of Science and Technology, Qingdao 266000, China; Feihu_Liu1123@163.com

2 Key Laboratory of Biofuels, Qingdao Institute of Bioenergy and Bioprocess Technology, Chinese Academy of Sciences, Qingdao 266101, China; wang_da@qibebt.ac.cn

3 College of Environmental Science and Engineering, Yangzhou University, Yangzhou 225127, China; chendan@yzu.edu.cn

* Correspondence: wangzhong@qibebt.ac.cn (Z.W.); chen-fushan@263.net (F.C.); lixb@qibebt.ac.cn (X.L.); Tel.: +86-1586-551-6166 (F.C.); +86-1586-687-0310 (Z.W. & X.L.)

† These authors contributed equally to this work.

Received: 1 February 2019; Accepted: 19 March 2019; Published: 21 March 2019

Abstract: The CeO_2 ordinary amorphous, nanopolyhedrons, nanorods, and nanocubes were prefabricated by the hydrothermal method, and employed as carriers of Fe/W–CeO_2 catalysts to selectively catalyze the reduction of NO with ammonia. Characterization results indicated that the morphology of CeO_2 support originated from selectively exposing different crystal surfaces, which has a significant effect on oxygen vacancies, acid sites and the dispersion of Fe_2O_3. The CeO_2 nanopolyhedrons catalyst (Fe/W–CeO_2–P) showed most oxygen vacancies, the largest the quantity of acid sites, the largest BET (Brunauer-Emmett-Teller) surface area and the best dispersion of Fe_2O_3, which was associated with predominately exposing CeO_2 (111) planes. Consequently, the Fe/W–CeO_2–P catalyst has the highest NO conversion rate in the temperature range of 100–325 °C among the ordinary amorphous, nanorods, and nanocubes Fe/W–CeO_2 catalysts.

Keywords: morphology; Fe/W–CeO_2; nanopolyhedra; CeO_2 (111) planes

1. Introduction

As one of the main atmospheric pollutants, nitrogen oxides (NO_x) can cause acid rain and photochemical smog, which are pernicious to the environment and human health [1–3]. At present, the most effective method for treating stationary sources nitrogen oxides is mainly the selective catalytic reduction of nitrogen oxides with NH_3 (NH_3-SCR) [4,5]. Different kinds of inorganic metal oxides, such as MnO_x, CeO_2, and Fe_2O_3, cause great influence because of their high activity and high selectivity for NO_x reduction [6,7].

So far, more and more interest has been made in the study of the inorganic metals facet-dependent catalytic activities and inorganic metal oxide nanocatalysts, as it is known that the arrangement of atoms on the surface is directly correlation with catalytic reactivity. Inorganic metal oxide nanocrystals containing Co_3O_4 (110) nanorods [8], CeO_2 (110) sheets/CeO_2 (110)/(100) nanorods [9–11], TiO_2 (001) nanobelts [12–14], and Cu_2O (111) polyhedron/Cu_2O (110) rhombic dodecahedra [15,16] have also been found to show great superiority in catalytic activity in different reactions, because of the priority exposure of reactive faces in catalytic surfaces. These catalysts are exposed to a certain reaction surface and provide a reference for establishing a practical model for the basic research of heterogeneous catalysis, which are comparable to single crystal catalysts.

In addition to loading precious metal catalysts, ceria, the well-known functional rare-earth metal material, has also been used in NH_3-SCR. This is because its high oxygen storage capacity is related to the oxygen-rich vacancies and the low redox potential between Ce^{4+} and Ce^{3+}. Theoretical and experimental studies have shown that the dense CeO_2 (111) face is the most stable (thus inherently less reactive); CeO_2 (110) and (100) has lower stability [17]. Therefore, understanding the relationship between the structure and relative stability of CeO_2 faces can provide profound insights into catalytic reactions that typically occur on the surface. It is currently believed that the NH_3-SCR in ceria-based catalysts has been greatly enhanced, and a large number of studies have investigated catalytically active sits, oxygen vacancies, and metal-support interactions [18].

Therefore, the major purpose of the present study was to evaluate the relationship between the structural feature and activity of Fe/W–CeO_2 catalysts with different morphology. We prefabricated CeO_2 ordinary, nanopolyhedra, nanorods, and nanocubes with various exposed crystallographic facets by hydrothermal methods. Then the resulting powders were characterized by X-ray diffraction (XRD), transmission electron microscopy (TEM), Raman spectroscopy, diffuse reflectance UV–VIS spectroscopy (UV–VIS), Pyridine Fourier Transform Infrared Spectroscopy (Py-IR) and X-ray photoelectron spectroscopy (XPS).

2. Results

2.1. TEM and HRTEM Analysis

The morphology and microstructures of the CeO_2 and Fe/W–CeO_2 were conducted by TEM and HRTEM (high-resolution transmission electron microscopy) in Figure 1. It was found that CeO_2 catalyst of A, B, C, D showed ordinary morphology (A1), nanopolyhedrons (B1), nanorods (C1) and nanocubes (D1) in morphology, which denoted as CeO_2–O, CeO_2–P, CeO_2–R and CeO_2–C, respectively [11]. In particular, the morphology of CeO_2–O includes polyhedrons and ellipsoids. After impregnating Fe and W over the CeO_2 carrier, no significant change of the morphology was noticed, so the Fe/W-CeO_2 catalysts with different morphology were prepared. The size of CeO_2–O, CeO_2–P, and CeO_2–C were about 10 nm, 8 nm, and 40 nm. Additionally, CeO_2–R showed shape with 27–150 nm in length and 5–10 nm in width.

The HRTEM image in Figure 1 shows the lattice spacings of 0.31, 0.27, and 0.19 nm, matching well with the (111), (110) and (100) planes of CeO_2 for Fe/W–CeO_2–P, Fe/W–CeO_2–R, and Fe/W–CeO_2–C catalysts, respectively [11,19]. For Fe/W–CeO_2–O catalyst, it exposed three crystalline planes including CeO_2(111), CeO_2(100) and CeO_2(111). These observations indicated that the different preparation of CeO_2 support could expose different CeO_2 crystal plane [20]. Furthermore, all Fe/W–CeO_2 catalysts can be observed with the well-solved periodic lattice fringe of 0.25 nm consisting of the interplanar distance of the α-Fe_2O_3 (110) plane. As reported by Prieto-Centurion and Eaton et al. [21], similar α-Fe_2O_3 (110) structures on a CeO_2 support were also presented. Especially, all Fe/W–CeO_2 catalysts were measured lattice spacing of 0.29 nm to index to the $FeWO_4$ (111) crystal plane. Qu [22] et al. also proposed that the $FeWO_4$ species was formed in $Fe_{1-x}W_xO_\delta$ catalysts, which could provide Brønsted acid sites on account of the formation NH^{4+} as highly active species. These can express that different CeO_2 crystal faces did not affect the exposure of iron and tungsten crystal faces.

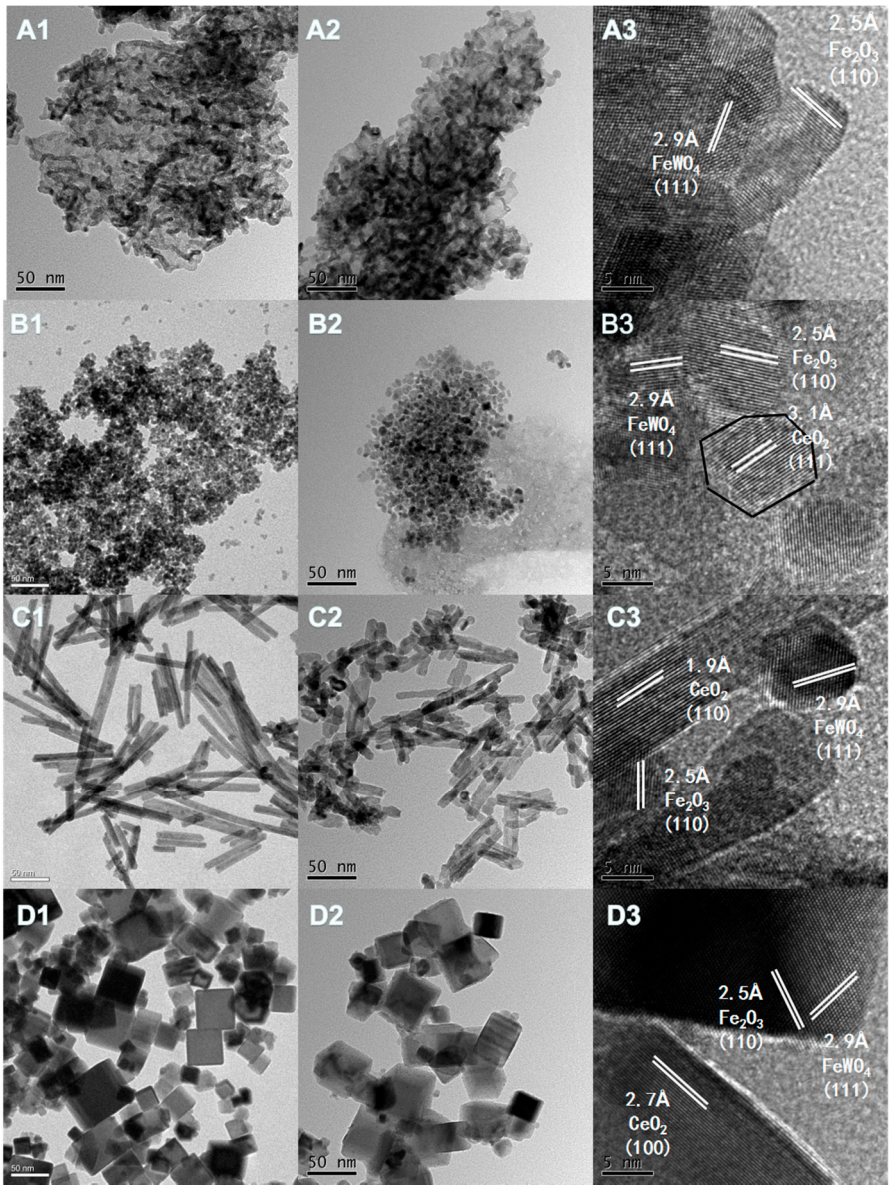

Figure 1. TEM images of (**A1**, **B1**, **C1** and **D1**) of CeO_2–O, CeO_2–P, CeO_2–R and CeO_2–C; TEM and HRTEM images of Fe/W–CeO_2–O (**A2** and **A3**), Fe/W–CeO_2–P (**B2** and **B3**), Fe/W–CeO_2–R (**C2** and **C3**) and Fe/W–CeO_2–C (**D2** and **D3**).

2.2. XRD

As shown in Figure 2, only the typical diffraction peaks of fluorite cubic structure were observed in as-synthesized materials. The diffraction peaks at 28.6°, 33.0°, 47.5°, 56.4°, 59.1°, 69.4°, 76.9°, and 79.4° can be attributed to (111), (200), (220), (311), (222), (400), (331), and (420) of the facets of CeO_2 (JCPDS card no. 43-1002), respectively. The wider reflection peak of the Fe/W–CeO_2–P indicated a small crystallite size compared with that of Fe/W–CeO_2–C, Fe/W–CeO_2–R and Fe/W–CeO_2–O catalysts [23,24]. The average crystalline sizes of Fe/W–CeO_2 were calculated from the CeO_2 (111) plane using Scherrer's formula. The results (Table 1) indicated that the order of crystallite size was similar to that of result of TEM. In the XRD measurement, the (011), (110), and (111) peaks of $FeWO_4$ should be at 2θ = about 23.7°, 24.9°, and 30.1°, respectively [25]. From the XRD comparison figure of CeO_2 and Fe/W–CeO_2, it is known that the peak intensity near 2θ = 20° − 35° is enhanced with the load of iron and tungsten in Figure S1. Therefore, it is reasonable to assume that a new phase of $FeWO_4$ formed with the addition of Fe/W species. It was clearly found that diffraction peaks of ferric

oxide and tungsten oxide were not detected in the materials. According to the results of XRD and HRTEM, it was obtained that Fe_2O_3 and $FeWO_4$ species might be highly dispersed on the surface of CeO_2 support.

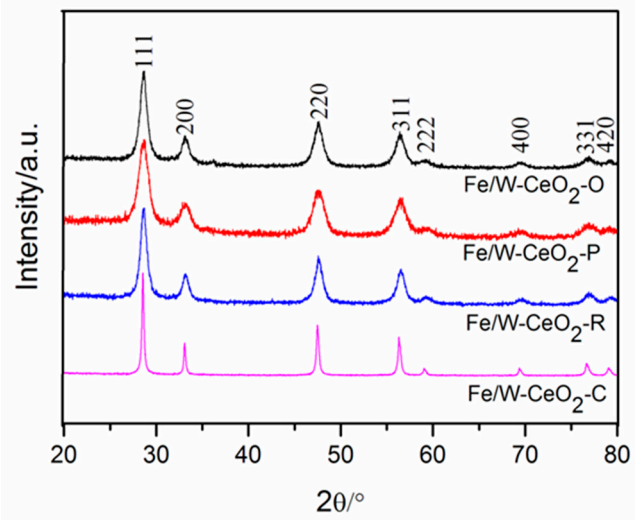

Figure 2. XRD patterns of Fe/W–CeO_2 catalysts.

Table 1. Physical properties of Fe/W–CeO_2 catalysts.

Samples	S_{BET} [a] (m^2 g^{-1})	V_{BJH} [b] (cm^3 g^{-1})	D_{BJH} [c] (nm)	Crystallite Size [d] (nm)	$S_{t\text{-}plot}$ [e] (m^2 g^{-1})
Fe/W–CeO_2–O	67.03	0.21	10.69	9.5	7.35
Fe/W–CeO_2–P	80.06	0.09	3.51	6.3	9.84
Fe/W–CeO_2–R	47.05	0.24	16.04	10.3	5.91
Fe/W–CeO_2–C	15.75	0.12	28.95	36.5	2.15

[a] BET surface area; [b] BJH desorption pore volume; [c] Average pore diameter.; [d] Calculated from the ceria (111) plane using Scherrer's formula.; [e] t-plot micropore area.

2.3. BET

It was seen that all samples could be divided into the type IV adsorption-desorption isotherm (Figure 3), revealing their mesoporous characteristics, which could be obtained from the packing of the nanoparticles. Fe/W–CeO_2–O, Fe/W–CeO_2–R, and Fe/W–CeO_2–C displayed H3 type hysteresis loop and verifed the existence of slit-shaped pores [26,27]. Especially, Fe/W–CeO_2–P also possessed an H4-type hysteresis loop at a relatively lower pressure, which can be explained by the interaction of cerium and iron leading to the formation of micropores. Additionally, the BET surface areas, pore volumes, and average pore diameter of the samples are summarized in Table 1. The pore distribution of Fe/W–CeO_2–P catalytic showed the least average pore size of 0.09 nm and the least average pore diameter of 3.51 nm, which indicated that Fe/W–CeO_2–P had porous structures. The porosity observed may be the interaction of iron and strontium to form some micropores for presence of intercrystalline voids between the nanocrystallites, which can be demonstrated by the values of micropore surface area. Moreover, Fe/W–CeO_2–P had the larger BET surface area and micropore surface area, resulting in high dispersion of the metal oxide composite with Fe/W [28]. The excellent dispersion of Fe/W–CeO_2–P was responsible for the smaller crystal size, consistent with HRTEM and XRD.

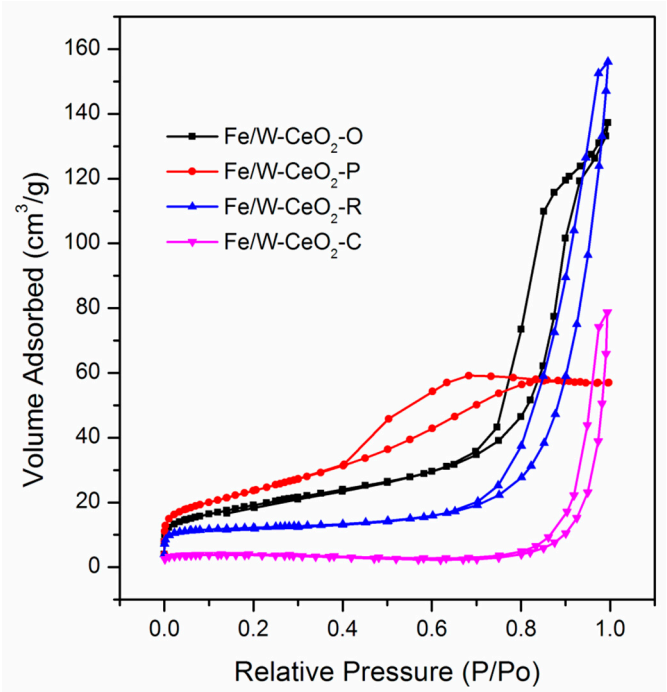

Figure 3. Nitrogen adsorption/desorption isotherms of Fe/W–CeO_2.

2.4. Raman

Figure 4 displays the visible Raman spectra of CeO_2 and Fe/W–CeO_2 catalysts. For the CeO_2 support, the distinct F_{2g} symmetry mode of the CeO_2 phase centered at 463 cm^{-1} with weak bands at 251, 600 and 1050 cm^{-1} assigned to the second-order transverse acoustic (2TA), defect-induced (D), and second-order longitudinal (2LO), respectively [29–31]. The Raman spectra for the Fe/W–CeO_2 structure almost remained after the addition of Fe and W species in Figure 4b. In addition, the peak at 251, 463, and 590 cm^{-1} in CeO_2 shifted to 247, 460, and 594 cm^{-1} in Fe/W–CeO_2, respectively. The peak at 1050 cm^{-1} shifted to 1170 cm^{-1} and was broadened. These shifts and broadening were attributed to the Fe or W addition into the CeO_2 lattice, which was related to the existence of reduced states of cerium. The results further implied the combination of Fe or W ions into the surface/subsurface of ceria without resulting in a change in the original cubic structure, which was consistent with XRD and TEM results.

Furthermore, the I_{600}/I_{460} values (the ratio of the intensities of the D and F2g bands) indicated the oxygen vacancies concentration (Figure 4c). The oxygen vacancies concentration followed the order: CeO_2–P > CeO_2–O > CeO_2–C > CeO_2–R. After the impregnation of Fe and W, all of the I_{600}/I_{460} values increased significantly. Moreover, the amount sequence of the oxygen vacancies over Fe/W–CeO_2 was consistent with the similar trend of pure CeO_2. Consequently, Fe or W insertion into the CeO_2 lattice might induce the increase in defect concentration in the nanostructure ceria [32].

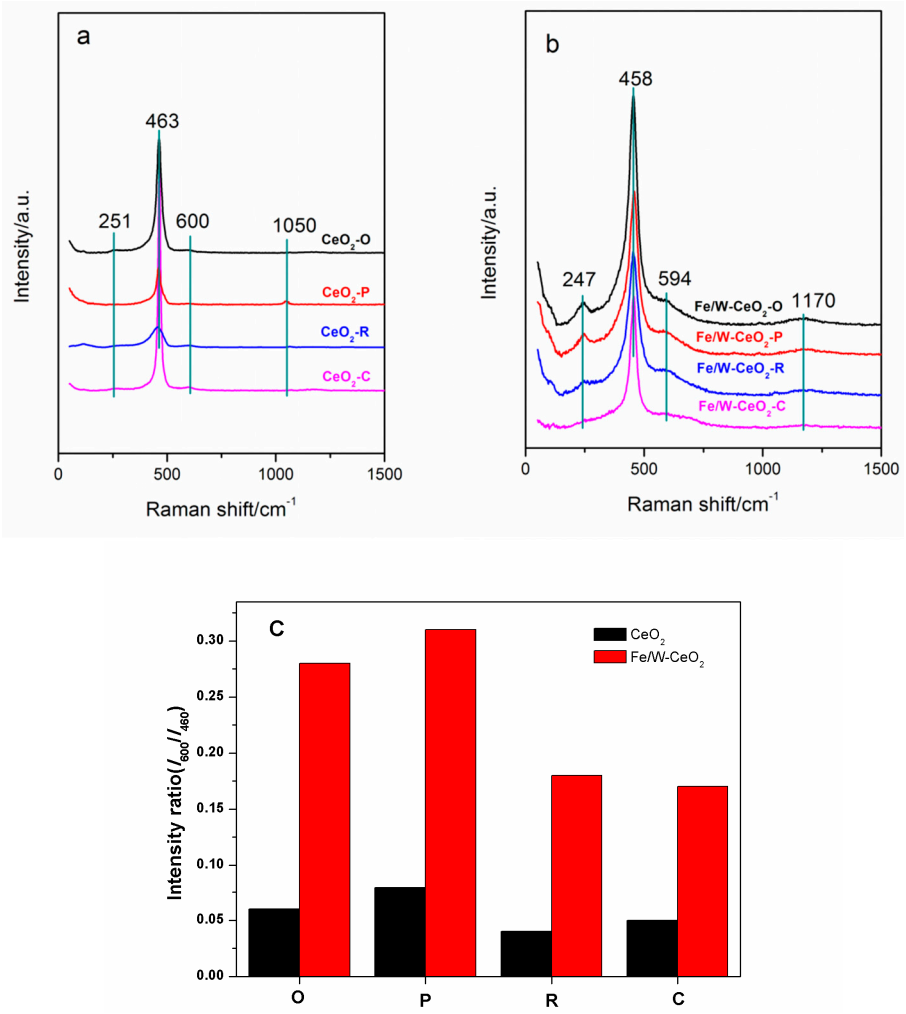

Figure 4. Raman spectra of (**a**) CeO_2, (**b**) Fe/W-CeO_2 ordinary, nanopolyhedra, nanorods, nanocubes, and (**c**) the corresponding peak intensity ratios I_{600}/I_{460}.

2.5. XPS

Ce3d spectra are presented in Figure 5a. The Ce^{4+} has been matched with six peaks: v (882.2 eV), v_2 (889.5 eV), v_3 (898.2 eV), u (901.2 eV), u_2 (907.7 eV) and u_3 (916.7 eV). Ce^{3+} has been fitted with two peaks: v_1 (885.1 eV) and u_1 (903.6 eV) [33]. The surface atomic concentrations of Ce^{3+} to the total Ce^{3+} and Ce^{4+} on the Fe/W–CeO_2–O, Fe/W–CeO_2–P, Fe/W–CeO_2–R and Fe/W–CeO_2–C were 0.18, 0.20, 0.15, and 0.14, respectively. This indicated that the oxygen vacancies of the Fe/W–CeO_2–P was more than those of Fe/W–CeO_2–O, Fe/W–CeO_2–R, and Fe/W–CeO_2–C, which is in agreement with the result of the oxygen vacancies by Raman. Oxygen vacancies can be generated by the transformation between Ce^{3+} and Ce^{4+} according to the following: $4Ce^{4+} + O^{2-} \rightarrow 4Ce^{4+} + 2e^- / \square + 0.5O_2 \rightarrow 2Ce^{4+} + 2Ce^{3+} + \square + 0.5O_2$, where $\square$ represented an empty position (anion-vacant site) originating from the removal of O^{2-} from the lattice [34]. The higher the Ce^{3+} concentration to the total Ce^{3+} and Ce^{4+} present, the more oxygen vacancies formed.

Figure 5b shows the characteristic peaks of the low binding energy iron-containing catalyst assigned to Fe $2p_{3/2}$. All the catalysts showed the Fe $2p_{3/2}$ peak and the corresponding peak at 714.7–715.2 eV and 717.8–718.4 eV, which was assigned to Fe^{2+} and Fe^{3+}, respectively [26,35]. The Fe^{2+} sites were formed by the interaction between Fe_2O_3 and CeO_2 support, probably through an interfacial redox process: $xFe_2O_3 + (2 - y)CeO_{2-x} \rightarrow xFe_2O_{3-y} + (2 - y)CeO_2$ [36]. According to the calculation of $Fe^{2+}/(Fe^{2+} + Fe^{3+})$ (Table 2), the concentration of Fe^{3+} decreased according to the sequence: Fe/W–CeO_2–P > Fe/W–CeO_2–O > Fe/W–CeO_2–C > Fe/W–CeO_2–R. Notably, Fe/W–CeO_2–P proved

obviously more Fe^{2+} species than other Fe/W–CeO_2, indicating there was strong Fe–Ce interfacial interaction over nanopolyhedrons CeO_2 support [37]. Moreover, these peaks were shifted to higher binding energy compared with that of pure Fe_2O_3 species, which was ascribed to the strong electron interaction between iron and tungsten. W4f spectra are presented in Figure 5c. Similar peaks of binding energy of $W4f_{7/2}$ (34.6–34.9 eV) and $W4f_{5/2}$ (36.6–36.9 eV) were observed over all the Fe/W–CeO_2 samples. These binding energies on Fe/W–CeO_2 catalysts were indeed lower than the corresponding values on original W^{6+} sample ($W4f_{7/2}$ at 35.8 eV and $W4f_{5/2}$ at 38.0 eV) [38,39]. This phenomenon should be related to the formation of $FeWO_4$ species (Figure 1) with electronic defects, which resulted in the increment of electron cloud of W^{6+} species. Feng et al. [40] also observed that the as-prepared monolayer-dispersed WO_x species on α-Fe_2O_3 surface had mixed oxidation states of W^{6+} and W^{5+}.

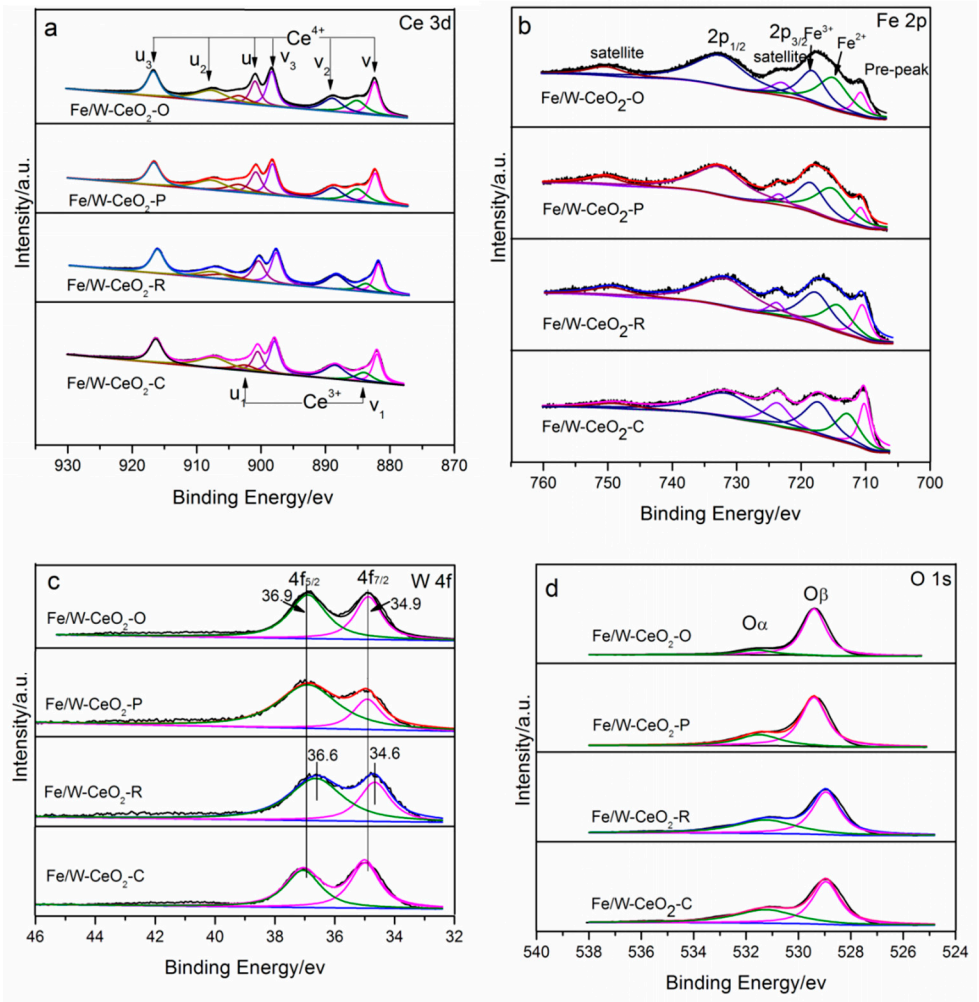

Figure 5. XPS spectra of (**a**) Fe 2p, (**b**) Ce 3d, (**c**) W 4f, and (**d**) O 1s for Fe/W–CeO_2 catalysts.

Table 2. Surface atomic concentration.

Samples	Fe/W	$Ce^{3+}/(Ce^{3+} + Ce^{4+})$	$O_\alpha/(O_\alpha + O_\beta)$	$Fe^{2+}/(Fe^{2+} + Fe^{3+})$
Fe/W–CeO_2–O	0.073	0.18	0.13	0.54
Fe/W–CeO_2–P	0.092	0.20	0.26	0.56
Fe/W–CeO_2–R	0.083	0.15	0.41	0.43
Fe/W–CeO_2–C	0.063	0.14	0.27	0.42

2.6. UV–VIS Diffuse Reflectance Spectra

Figure 6 reveals the UV–VIS absorption spectra of Fe/W–CeO_2 catalysts. Subbands around 215 and 276 nm arise from isolated Fe^{3+} sites in tetrahedral and higher coordination (five or six oxygen ligands), respectively. A broad band between 300 and 400nm in all catalyst can be deconvoluted into subbands at 316 nm, which was assigned to small oligomeric Fe_xO_y clusters. In addition, an additional shoulder peak at around 365 nm was attributed to WO_3 [41], which further proofed of the XPS results about the W^{6+} existence. Meanwhile, subbands > 400 nm (centered at around 521 nm) was assigned to large Fe_2O_3 particles [42], which was consistent with HRTEM results. This peak can be related to the degree of dispersion of metal. The stronger intensity absorption band of Fe_2O_3 was detected, suggesting that iron was in highly dispersive state, no large iron oxide particles aggregated in the sample [43,44]. It was noted that the Fe/W–CeO_2–P catalyst showed the weakest intensity peak of Fe_2O_3, suggesting the highest dispersion of iron in Fe/W–CeO_2–P catalyst.

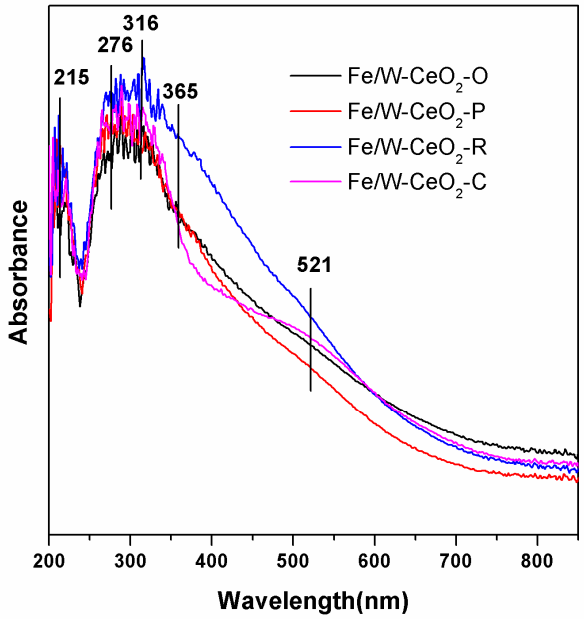

Figure 6. UV–VIS of Fe/W–CeO_2 catalysts.

2.7. Py-IR Spectra

Figure 7 shows the Py-IR spectra of three catalysts. Among these, the observed IR bands at 1441, 1574 and 1597 cm^{-1} correspond to different modes of vibration of pyridine coordinated to Lewis acid sites. The band at 1490 cm^{-1} was characteristic of the Lewis–Brønsted acid complex [45]. According to Emeis and Zhang et al. [46,47], the concentration of acid sites on four Fe/W–CeO_2 were calculated. In addition, the calculated results and the concentration of total acid sites of four catalysts followed the sequence of Fe/W–CeO_2–P (223 mmol/g) > Fe/W–CeO_2–O (207 mmol/g) > Fe/W–CeO_2–C (104 mmol/g) > Fe/W–CeO_2–R (31 mmol/g).

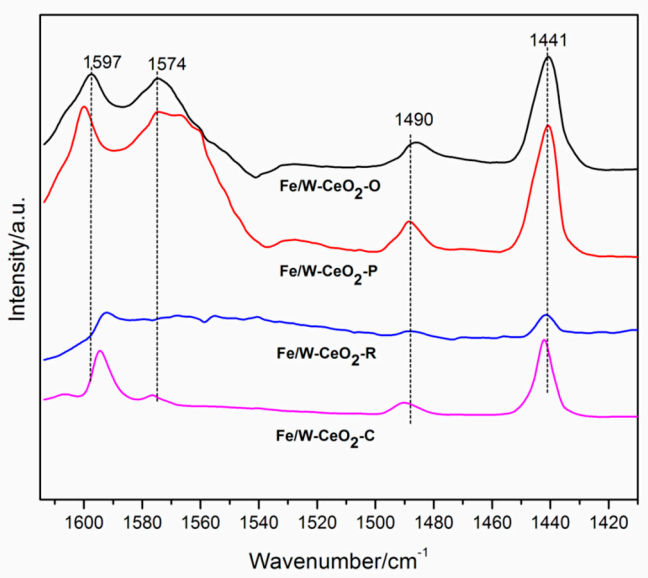

Figure 7. Py-IR spectra of four Fe/W–CeO_2 catalysts.

2.8. Activity Measurement

As is shown in Figure 8, the catalytic activity of NH_3-SCR on different morphological catalysts was investigated. It was obvious that the NO_x conversion over all Fe/W–CeO_2 increased first and decreased with the increase of temperature. Especially, the Fe/W–CeO_2–R line sharp rose from 20% up to 82% (the vertex) of NO_x conversion, which sudden dropped at 350 °C. The Fe/W–CeO_2–P displayed the highest NO_x conversion and the widest range of operating-temperature window between 225 and 325 °C. Among the four catalysts, the NO conversion efficiency decreased in the order: Fe/W–CeO_2–O > Fe/W–CeO_2–R > Fe/W–CeO_2–C. As shown in Figure 8b, all Fe/W–CeO_2 catalysts showed 100% N_2 selectivity below 225 °C. By increasing the reaction temperature, the N_2 selectivity decreased slightly, but it was still higher than 95%.

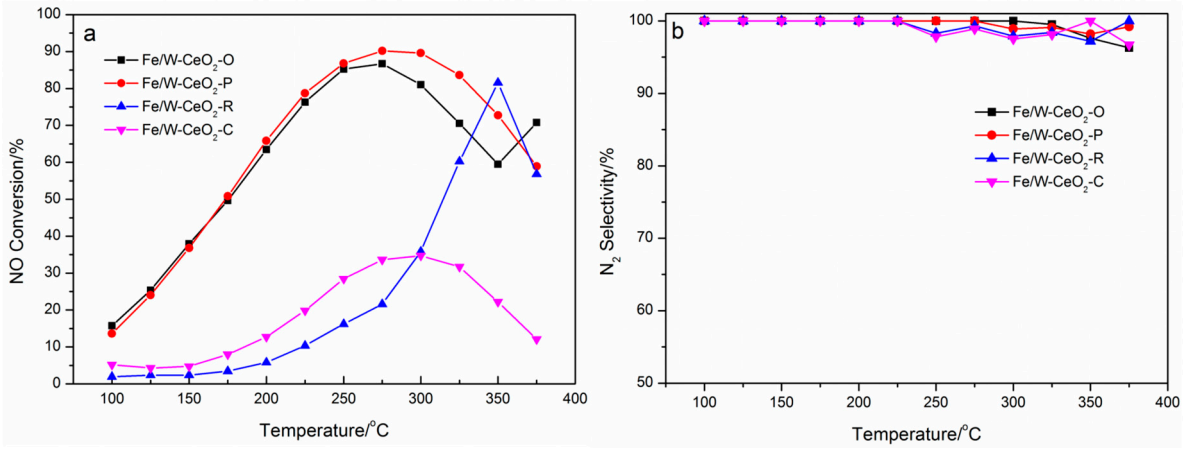

Figure 8. Different morphology Fe/W–CeO_2 catalysts of (**a**) NO conversions and (**b**) N_2 selectivity. Reaction conditions: [NO] = [NH_3] = 500 ppm, [O_2] = 3%, GHSV = 50,000 h^{-1} and Ar as balance gas.

The NO reaction rates for Fe/W–CeO_2–O, Fe/W–CeO_2–P, Fe/W–CeO_2–R, and Fe/W–CeO_2–C are 1.88×10^{-4} mol_{NO} g_{cat}^{-1} s^{-1}, 2.40×10^{-4} mol_{NO} g_{cat}^{-1} s^{-1}, 2.34×10^{-5} mol_{NO} g_{cat}^{-1} s^{-1}, and 3.97×10^{-5} mol_{NO} g_{cat}^{-1} s^{-1} at 150 °C, respectively. This value were in the order: Fe/W–CeO_2–P > Fe/W–CeO_2–O > Fe/W–CeO_2–C > Fe/W–CeO_2–R, representing that CeO_2 (111) was superior to CeO_2 (110) and (100) as a carrier for $FeWO_x$.

An Arrhenius plot in view of reaction rate data between 100 and 150 °C is displayed in Figure 9. The apparent activation energy of Fe/W–CeO_2–P was 36 kJ mol^{-1}, which is lower than that of Fe/W–CeO_2–O, Fe/W–CeO_2–R and Fe/W–CeO_2–C catalysts (41, 55 and 48 kJ mol^{-1}). Therefore, the catalytic performance of Fe/W–CeO_2–P catalyst was better than that of the Fe/W–CeO_2–O, Fe/W–CeO_2–R, and Fe/W–CeO_2–C catalysts. According to the references [48,49], it can draw a conclusion that the lower the apparent activation energy, the easier the reaction, so the Fe/W–CeO_2–P catalyst requires less energy in the reaction, indicating the excellent catalytic performance.

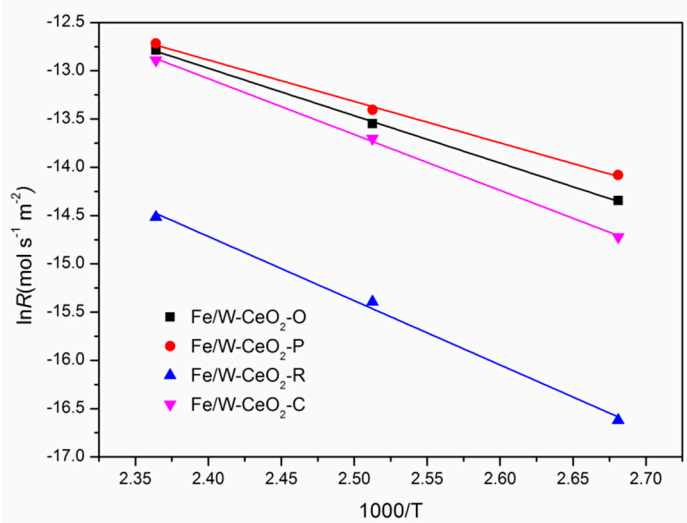

Figure 9. Arrhenius plots of the inherent reaction rate constants of Fe/W–CeO_2 catalysts.

2.9. The Effect of SO_2 and H_2O

The effect of extra gas streams of 200 ppm SO_2 and/or 5% H_2O on de-NO_x measurement with a constant temperature of 300 °C are shown in Figure 10. When the additional gas stream was turned on and off, the de-NO_x measurement remained constant for a few minutes. The NO conversion reduced from 90% to 86% after adding SO_2. After the addition of H_2O, the NO conversion reduced to 82%, and when SO_2 and H_2O were added at the same time, the NO conversion was about 75%. After removing the additional gas, in all three cases, the NO conversion returned to a value very close to the initial value. The above results indicated that Fe/W–CeO_2 showed excellent resistance of sulfur dioxide and water, which may be due to the addition of iron and tungsten mentioned in the literature. The addition of iron oxide significantly reduced the rate of sulfate formation, thereby inhibiting the progress of the reaction [50]. For tungsten oxide, it can reduce the stability of cerium sulfate, which occupied the active site of catalyst [51].

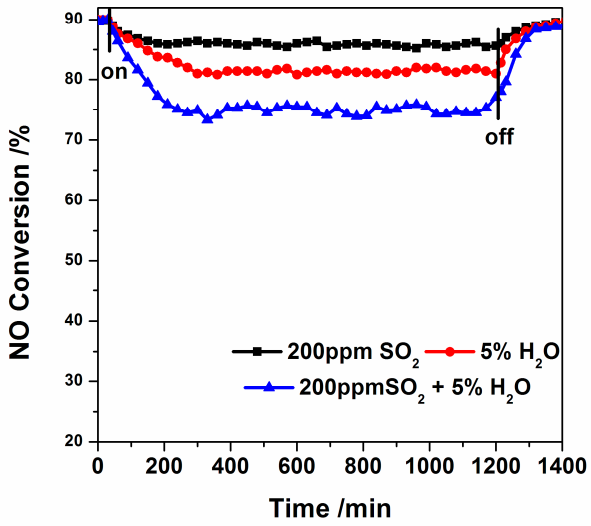

Figure 10. The effect of SO_2 and H_2O on NO conversion over Fe/W–CeO_2–P at 300 °C. Reaction conditions: [NO] = [NH_3] = 500 ppm, [O_2] = 3%, 200 ppm SO_2 (when used), 5 vol.% H_2O (when used), GHSV = 50,000 h^{-1}, and Ar as balance gas.

3. Discussion

The activities of four Fe/W–CeO_2 can be ranked: Fe/W–CeO_2–P > Fe/W–CeO_2–O > Fe/W–CeO_2–C > Fe/W–CeO_2–R at temperatures of 100–300 °C. On the one hand, the catalytic behavior of Fe/W–CeO_2–P and Fe/W–CeO_2–O is significantly different from that of Fe/W–CeO_2–R and Fe/W–CeO_2–C on the other hand. The former two are more active and their conversion curves cover the temperature range of 100 to 250 °C, although the Fe/W–CeO_2–P based catalyst has higher activity in the range of 250–300 °C. Both Fe/W–CeO_2–P and Fe/W–CeO_2–O have too many similarities in terms of morphology and exposed crystal faces. Therefore, in the subsequent oxygen vacancies, the BET specific surface area, the dispersion of iron oxide, and the amount of acid all have close performance, which is also reflected in the catalyst activity in the low temperature section. Additionally, the crystal faces may not be the main influencing factors of both. However, the difference in the preparation methods between Fe/W–CeO_2–P and Fe/W–CeO_2–O may be the main influencing factors [52–54], and the incomplete agreement among the exposed crystal faces leads to a significant difference in the catalytic activity in the high temperature range.

According to the above-mentioned characterization results, Fe/W–CeO_2–P catalyst possessed higher oxygen vacancies (XPS and Raman). In addition, Fe/W–CeO_2–P was exposed to more stable crystal plane with CeO_2 (111) plane (HRTEM) where low cation such as Ce^{3+} and Fe^{2+} was more likely to exist because they are not easily oxidized. For details, the spontaneous reduction of Ce^{4+} to Ce^{3+} was known to improve the formation of oxygen vacancies for maintaining electrostatic balance [55]. It was generally believed that oxygen migration in ceria-based materials was carried out through vacancy hopping mechanism [56]. Thus, Fe/W–CeO_2–P catalyst with the oxygen vacancies might was beneficial to oxygen migration and has more active oxygen than other catalysts.

The higher dispersion of iron in Fe/W–CeO_2–P catalyst are received by the results of XRD and UV–VIS. The a new active phase of Fe and Ce can enhanced the NO_x reduction performance [57]. By XPS, Fe/W–CeO_2–P present the higher Fe^{2+} concentration or a litter amount of Fe_2O_3, which may due to stable CeO_2 (111) plane. X-ray diffraction and UV–VIS spectroscopy results support the idea that a large amount of Fe_2O_3 in three other Fe/W–CeO_2 catalysts may cover the active side of CeO_2. This may explain the Fe/W–CeO_2–P good performs as one factor.

The BET results indicated that Fe/W–CeO_2–P had the relatively highest BET surface area and micropore surface area (Table 1), which could improve the strong synergism between iron and cerium (XPS) and the dispersion of Fe_2O_3 (UV–VIS). The acid sites in Fe_2O_3 could adsorb NH_3 and NO by

Langmuir-Hinshelwood mechanism. Then adsorbed species could be converted into corresponding intermediates, such as coordination NH_3 and NH^{4+} iron [58]. Therefore, the Fe/W–CeO_2–P with most amount of acid sites showed the best NH_3-SCR reaction performance.

4. Materials and Methods

4.1. Catalysts Preparation

The all chemicals were purchased from Aladdin Industrial Corporation (shanghai, China). The CeO_2 were prepared by a hydrothermal method, using $Ce(NO_3)_3{\cdot}6H_2O$ as the source of cerium and NaOH as the precipitant. The morphologies of CeO_2 nano-particles were governed by changing the concentration of NaOH, and the temperature of synthesis. The details in (1) $Ce(NO_3)_3{\cdot}6H_2O$ and NaOH were each dissolved in homemade deionized water. Then the above two solutions were mixed in a large beaker and kept stirring for 30 min to form the emulsion. Subsequently, the emulsion was poured into a Teflon bottle and hydrothermally treated at a temperature of 100 °C for 24 h, denoted as B; (2) The second catalyst only changes the concentration of NaOH to 6mol/L. The other conditions are the same as those of the B catalyst, denoted as C; (3) The third catalyst only adjusts the hydrothermal temperature to 180 °C. The other conditions are the same as the C catalyst preparation conditions, denoted as D. Then after the hydrothermal treatment, all fresh precipitates were separately separated by centrifugation, washed two or three times with homemade deionized water and pure ethanol, and dried overnight in air at 60 °C; (4) the $Ce(NO_3)_3{\cdot}6H_2O$ was directly calcined in static air by muffle furnace at 500 °C for 3 h at a ramping rate of 2 °C min^{-1} as the A catalyst. $Fe(NO_3)_3{\cdot}9H_2O$ was dissolved in the adequate oxalic acid ($H_2C_2O_4{\cdot}2H_2O$) solution, then ammonium metatungstate ($(NH_4)_6H_2W_{12}O_{40}{\cdot}xH_2O$) was added into the solution for W in portion. The loading of active phase F/W of the main four catalysts was 9.5 to 1.0 of molar ratio. These CeO_2 powders were impregnated with incipient wetness by the solution and dried at 70 °C overnight, which were calcined in static air by muffle furnace at 550 °C for 3 h with a ramping rate of 2 °C min^{-1} subsequently [59,60].

4.2. Characterizations of Catalysts

X-ray diffraction (XRD) measurements were performed on a Bruker (Billerica, MA, USA) AXS-D8. The advanced powder diffractometer is equipped with monochrome detector and CuKa radiation source. The diffraction patterns were recorded in the 2θ range of 20°–80° with a step size of 0.02°. The morphologies of the as-prepared samples were characterized by a field emission transmission electron microscope (TEM) of Tecnai G2 F20 (FEI, Hillsboro, OR, USA), dispersed into analytical purity alcohol with an ultrasound system before observation. Nitrogen adsorption/desorption measurements of the samples were accomplished on a surface analyzer (Micrometrics, ASAP 2020, Norcross, GA, USA) at 77K. The samples specific surface area was calculated using the Brunauer–Emmett–Teller (BET) method. The pore size distributions were determined from desorption branches by the Barrett–Joyner–Halenda (BJH) method. The chemical states of the atoms on the surface of the catalyst were investigated using a VG ESCALAB 210 electron spectrometer (Mg Kα radiation; hν = 1253.6eV, Thermo Fisher Scientific, Waltham, MA, USA). The XPS data were calibrated using the C1s (284.6 eV) binding energy as the standard. UV–VIS diffuse reflectance spectra were collected on a Shimadzu (Kyoto, Japan) UV 2550 spectrophotometer. The FTIR of pyridine (Py) was measured on Thermo Nicolet 6700 FTIR Spectrometer (Thermo Fisher Scientific, Waltham, MA, USA) with a resolution of 0.5 cm^{-1}.

4.3. Activity Measurement

The catalytic performance by a fixed-bed quartz tube reactor was evaluated. The gas composition of the 0.5 g Fe/W–CeO_2 sample was as follows: 500 ppm NO, 500 ppm NH_3, 3 vol.% O_2, Ar balance, and a total flow rate of 300 mL/min. Hence the corresponding gas hourly space velocity (GHSV) was 50,000 h^{-1}. The catalysts were pressed, comminuted and sieved to 20–40 mesh prior to each activity test,

then filled into a quartz pipe reactor with an inner diameter of 8 mm. At each temperature step of 25 °C between 100 to 375 °C, the concentrations of NO, NH_3 and N_2O were measured. The concentrations of NO in the inlet and outlet gases were measured using a 4000VM NOx analyzer. The concentrations of N_2O and NH_3 were measured by a G200 analyzer and an IQ 350 ammonia analyzer.

NO conversion was calculated according to the following equations:

$$NO\ Conversion\ (\%) = \frac{[NO]_{in} - [NO]_{out}}{[NO]_{in}} \times 100\% \quad (1)$$

$$N_2\ Selectivity\ (\%) = (1 - \frac{2[N_2O]_{out}}{[NO]_{in} - [NO]_{out} + [NH_3]_{in} - [NH_3]_{out}}) \times 100\% \quad (2)$$

In order to comprehend the intrinsic influence of the morphology of CeO_2 nanostructures on the Fe/W-CeO_2, the catalytic performance data were analyzed by the macroscopic kinetics. The NH_3-SCR on the Fe/W-CeO_2 was generally recognized to be a first-order reaction related to NO [61,62]. Kinetic experiments were implemented in a fixed-bed reactor. The NOx conversion was modified to below 40% so as to eliminate the thermal effect and diffusion effect before calculating the reaction rate which was normalized over the surface area and shown below:

$$k = \frac{FX}{W_c S_c} \quad (3)$$

where k is the reaction constant (mol s^{-1} m^{-2}), F is the molar NO feed rate (mol s^{-1}), X is the conversion of NO, W_c is the catalyst weight (g), (%), S_c is the catalyst BET surface area, and T is the temperature (K). The apparent activation energies (E_a) were calculated by the Arrhenius law (ln (k) = f (1000/T)).

5. Conclusions

Four Fe/W–CeO_2 with different ceria morphologies as supports were prefabricated by a hydrothermal method. The HRTEM images revealed that Fe/W–CeO_2–P, Fe/W–CeO_2–R, and Fe/W–CeO_2–C mainly exposed CeO_2 (111), (110), and (100) crystal planes, respectively. Characterization results showed that the morphology of CeO_2 support originated from selectively exposing different crystal surfaces. The Fe/W–CeO_2–P catalyst with more oxygen vacancies, more acid sites, the higher BET surface area and the best dispersion of Fe_2O_3, which exhibited better activity of NH_3-SCR. The CeO_2 (111) was the most inert crystal plane compared to the well-known reactive (110) and CeO_2 (100) planes. Therefore, the interface behavior and catalytic characteristics of Fe/W–CeO_2 catalysts for NO reduction was mainly on account of the morphology and crystal-plane effect and the synergistic effect between active species and supports.

Supplementary Materials: The following are available online at http://www.mdpi.com/2073-4344/9/3/288/s1, **Figure S1.** XRD patterns of Fe/W-CeO_2 and CeO_2 catalysts.

Author Contributions: Z.W., X.L., and F.C. conceived and designed the experiments; Z.W. and D.C. revised the paper; F.L. and D.W. analyzed the data; F.L. performed the experiments, and wrote the paper.

Funding: The work described above was supported by the National Natural Science Foundation of China (no: 21607162, 2157061214, 21676287), and the Natural Science Foundation of Shandong Province (no. ZR2017ZC0633).

Conflicts of Interest: The authors declare no conflict of interest.

References

1. Li, J.; Chang, H.; Ma, L.; Hao, J.; Yang, R.T. Low-temperature selective catalytic reduction of NOx with NH3 over metal oxide and zeolite catalysts: A review. *Catal. Today* **2011**, *175*, 147–156. [CrossRef]
2. Liu, G.; Gao, P.X. A review of NO_x storage/reduction catalysts: mechanism, materials and degradation studies. *Catal. Sci. Technol.* **2011**, *1*, 552–568. [CrossRef]
3. Wu, D.W.; Zhang, Q.L.; Lin, T.; Gong, M.C.; Chen, Y.Q. Effect of Fe on the Selective Catalytic Reduction of NO by NH_3 at Low Temperature over Mn/CeO_2-TiO_2 Catalyst. *J. Inorg. Mater.* **2012**, *27*, 495–500. [CrossRef]

4. Liu, Z.; Zhu, J.; Li, J.; Ma, L.; Woo, S.I. Novel Mn–Ce–Ti Mixed-Oxide Catalyst for the Selective Catalytic Reduction of NO_x with NH_3. *ACS Appl. Mater. Interfaces* **2014**, *6*, 14500–14508. [CrossRef] [PubMed]
5. Zhang, X.; Lv, X.; Shi, X.; Yang, Y.; Yang, Y. Enhanced hydrophobic UiO-66 (University of Oslo 66) metal-organic framework with high capacity and selectivity for toluene capture from high humid air. *J. Colloid Interface Sci.* **2018**, *539*, 152–160. [CrossRef]
6. Liu, F.; Yu, Y.; He, H. Environmentally-benign catalysts for the selective catalytic reduction of NO_x from diesel engines: structure-activity relationship and reaction mechanism aspects. *Chem. Commun.* **2014**, *50*, 8445–8463. [CrossRef]
7. Zhang, X.; Yang, Y.; Lv, X.; Wang, Y.; Liu, N.; Chen, D.; Cui, L. Adsorption/desorption kinetics and breakthrough of gaseous toluene for modified microporous-mesoporous UiO-66 metal organic framework. *J. Hazard. Mater.* **2018**, *366*, 140–150. [CrossRef]
8. Xie, X.; Yong, L.; Liu, Z.Q.; Haruta, M.; Shen, W.J.C. ChemInform Abstract: Low-Temperature Oxidation of CO Catalyzed by Co_3O_4 Nanorods. *Nature* **2010**, *40*, 746–749. [CrossRef]
9. Sun, Y.; Liu, Q.; Gao, S.; Cheng, H.; Lei, F.; Sun, Z.; Jiang, Y.; Su, H.; Wei, S.; Xie, Y. Pits confined in ultrathin cerium(IV) oxide for studying catalytic centers in carbon monoxide oxidation. *Nature Commun.* **2013**, *4*. [CrossRef]
10. Zhou, K.B.; Wang, X.; Sun, X.M.; Peng, Q.; Li, Y.D. Enhanced catalytic activity of ceria nanorods from well-defined reactive crystal planes. *J. Catal.* **2005**, *229*, 206–212. [CrossRef]
11. Mai, H.X.; Sun, L.D.; Zhang, Y.W.; Si, R.; Feng, W.; Zhang, H.P.; Liu, H.C.; Yan, C.H. Shape-selective synthesis and oxygen storage behavior of ceria nanopolyhedra, nanorods, and nanocubes. *J. Phys. Chem. B* **2005**, *109*, 24380–24385. [CrossRef]
12. Yang, H.G.; Liu, G.; Qiao, S.Z.; Sun, C.H.; Jin, Y.G.; Smith, S.C.; Zou, J.; Cheng, H.M.; Lu, G.Q. Solvothermal Synthesis and Photoreactivity of Anatase TiO_2 Nanosheets with Dominant {001} Facets. *J. Am. Chem. Soc.* **2009**, *131*, 4078–4083. [CrossRef]
13. Yang, H.G.; Sun, C.H.; Qiao, S.Z.; Zou, J.; Liu, G.; Smith, S.C.; Cheng, H.M.; Lu, G.Q. Anatase TiO_2 single crystals with a large percentage of reactive facets. *Nature* **2008**, *453*, 638–641. [CrossRef]
14. Boningari, T.; Pappas, D.K.; Smirniotis, P.G. Metal oxide-confined interweaved titania nanotubes M/TNT (M = Mn, Cu, Ce, Fe, V, Cr, and Co) for the selective catalytic reduction of NO_x in the presence of excess oxygen. *J. Catal.* **2018**, *365*, 320–333. [CrossRef]
15. Hua, Q.; Cao, T.; Gu, X.K.; Lu, J.; Jiang, Z.; Pan, X.; Luo, L.; Li, W.X.; Huang, W. Crystal-Plane-Controlled Selectivity of Cu_2O Catalysts in Propylene Oxidation with Molecular Oxygen. *Angew. Chem. Int. Ed.* **2014**, *53*, 4856–4861. [CrossRef]
16. Laursen, S.; Combita, D.; Hungria, A.B.; Boronat, M.; Corma, A. First-Principles Design of Highly Active and Selective Catalysts for Phosgene-Free Synthesis of Aromatic Polyurethanes. *Angew. Chem. Int. Ed.* **2012**, *51*, 4190–4193. [CrossRef]
17. Montini, T.; Melchionna, M.; Monai, M.; Fornasiero, P. Fundamentals and Catalytic Applications of CeO2-Based Materials. *Chem. Rev.* **2016**, *116*, 5987–6041. [CrossRef]
18. Damma, D.; Boningari, T.; Ettireddy, P.R.; Reddy, B.M.; Smirniotis, P.G. Direct Decomposition of NO_x over TiO_2 Supported Transition Metal Oxides at Low Temperatures. *Ind. Eng. Chem. Res.* **2018**, *57*, 16615–16621. [CrossRef]
19. Wang, Z.L.; Feng, X.D. Polyhedral shapes of CeO_2 nanoparticles. *J. Phys. Chem. B* **2003**, *107*, 13563–13566. [CrossRef]
20. Zhang, X.; Hou, F.; Yang, Y.; Wang, Y.; Ning, L.; Dan, C.; Yang, Y.Q. A facile synthesis for cauliflower like CeO_2 catalysts from Ce-BTC precursor and their catalytic performance for CO oxidation. *Appl. Surf. Sci.* **2017**, *423*, 771–779. [CrossRef]
21. Prieto-Centurion, D.; Eaton, T.R.; Roberts, C.A.; Fanson, P.T.; Notestein, J.M. Catalytic reduction of NO with H_2 over redox-cycling Fe on CeO_2. *Appl. Catal. B Environ.* **2015**, *168–169*, 68–76. [CrossRef]
22. Wang, H.; Qu, Z.; Dong, S.; Xie, H.; Tang, C.J. Superior Performance of $Fe_{1-x}W_xO_\delta$ for the Selective Catalytic Reduction of NO_x with NH_3: Interaction between Fe and W. *Environ. Sci. Technol.* **2016**, *50*, 13511. [CrossRef] [PubMed]
23. Huang, X.S.; Sun, H.; Wang, L.C.; Liu, Y.M.; Fan, K.N.; Cao, Y. Morphology effects of nanoscale ceria on the activity of Au/CeO_2 catalysts for low-temperature CO oxidation. *Appl. Catal. B Environ.* **2009**, *90*, 224–232. [CrossRef]

24. Pan, C.; Zhang, D.; Shi, L. Template-Free Synthesis, Controlled Conversion, and CO Oxidation Properties of CeO_2 Nanorods, Nanotubes, Nanowires, and Nanocubes. *Eur. J. Inorg. Chem.* **2008**, *15*, 2429–2436. [CrossRef]
25. Zhang, J.; Zhang, Y.; Yan, J.Y.; Li, S.K.; Wang, H.S.; Huang, F.Z.; Shen, Y.H.; Xie, A.J. A novel synthesis of star-like $FeWO_4$ nanocrystals via a biomolecule-assisted route. *J. Nanopart. Res.* **2012**, *14*, 1–10. [CrossRef]
26. Liu, F.; He, H. Structure-Activity Relationship of Iron Titanate Catalysts in the Selective Catalytic Reduction of NO_x with NH_3. *J. Phys. Chem. C* **2010**, *114*, 16929–16936. [CrossRef]
27. Zhang, Q.; Song, Z.; Ning, P.; Liu, X.; Li, H.; Gu, J. Novel promoting effect of acid modification on selective catalytic reduction of NO with ammonia over CeO2 catalyst. *Catal. Commun.* **2015**, *59*, 170–174. [CrossRef]
28. Zhang, X.; Hou, F.; Li, H.; Yang, Y.; Wang, Y.; Liu, N.; Yang, Y. A strawsheave-like metal organic framework Ce-BTC derivative containing high specific surface area for improving the catalytic activity of CO oxidation reaction. *Microporous Mesoporous Mater.* **2018**, *259*, 211–219. [CrossRef]
29. Hao, Y.; Wang, Y.; Wang, L.; Ni, Z.; Wang, Z.; Wang, R.; Koo, C.K.; Shen, Z.; Thong, J.T.L. Probing Layer Number and Stacking Order of Few-Layer Graphene by Raman Spectroscopy. *Small* **2010**, *6*, 195–200. [CrossRef]
30. Wu, Z.; Li, M.; Howe, J.; Meyer, H.M., III; Overbury, S.H. Probing Defect Sites on CeO_2 Nanocrystals with Well-Defined Surface Planes by Raman Spectroscopy and O_2 Adsorption. *Langmuir* **2010**, *26*, 16595–16606. [CrossRef]
31. Li, Y.; Wei, Z.; Gao, F.; Kovarik, L.; Peden, C.H.F.; Wang, Y. Effects of CeO_2 support facets on VO_x/CeO_2 catalysts in oxidative dehydrogenation of methanol. *J. Catal.* **2014**, *315*, 15–24. [CrossRef]
32. Zhang, X.; Yang, Y.; Liang, S.; Wang, Y.; Chi, H.; Zhong, W.; Cui, L.J. High and stable catalytic activity of Ag/Fe_2O_3 catalysts derived from MOFs for CO oxidation. *Mol. Catal.* **2018**, *447*, 80–89. [CrossRef]
33. Larachi, F.; Pierre, J.; Adnot, A.; Bernis, A. Ce 3d XPS study of composite CexMn1-xO2-y wet oxidation catalysts. *Appl. Surf. Sci.* **2002**, *195*, 236–250. [CrossRef]
34. Liu, X.; Zhou, K.; Wang, L.; Wang, B.; Li, Y. Oxygen Vacancy Clusters Promoting Reducibility and Activity of Ceria Nanorods. *J. Am. Chem. Soc.* **2009**, *131*, 3140–3141. [CrossRef]
35. Grosvenor, A.P.; Kobe, B.A.; Biesinger, M.C.; Mcintyre, N.S.; Analysis, I. Investigation of Multiplet Splitting of Fe 2p XPS Spectra and Bonding in Iron Compounds. *Surf. Interface Anal.* **2004**, *36*, 1564–1574. [CrossRef]
36. Wang, H.; Jin, B.; Wang, H.; Ma, N.; Wei, L.; Duan, W.; Wu, X.; Shuang, L.J. Study of Ag promoted $Fe_2O_3@CeO_2$ as superior soot oxidation catalysts: The role of Fe_2O_3 crystal plane and tandem oxygen delivery. *Appl. Catal. B Environ.* **2018**, *237*, 251–262. [CrossRef]
37. Xiaodong, Z.; Xialu, Z.; Liang, S.; Fulin, H.; Yiqiang, Y.; Yuxin, W.; Ning, L.J. Enhanced catalytic performance for CO oxidation and preferential CO oxidation over CuO/CeO_2 catalysts synthesized from metal organic framework: Effects of preparation methods. *Int. J. Hydrogen Energy* **2018**, *43*, 18279–18288. [CrossRef]
38. Liu, F.; Shan, W.; Lian, Z.; Liu, J.; Hong, H.J. The smart surface modification of Fe_2O_3 by WO_x for significantly promoting the selective catalytic reduction of NO_x with NH_3. *Appl. Catal. B Environ.* **2018**, *230*. [CrossRef]
39. Liu, Z.; Liu, Y.; Li, Y.; Su, H.; Ma, L. WO_3 promoted Mn–Zr mixed oxide catalyst for the selective catalytic reduction of NO_x with NH_3. *Chem. Eng. J.* **2016**, *283*, 1044–1050. [CrossRef]
40. Feng, Z.; Kim, C.Y.; Elam, J.W.; Ma, Q.; Zhang, Z.; Bedzyk, M.J. Direct atomic-scale observation of redox-induced cation dynamics in an oxide-supported monolayer catalyst: WO_x/α-$Fe_2O_3(0001)$. *J. Am. Chem. Soc.* **2009**, *131*, 18200–18201. [CrossRef]
41. Si, Z.; Wu, X.; Duan, W.; Ma, Z.; Jing, M.J. Tailored temperature window of CuO_x/WO_x–ZrO_2 for NO_x reduction via adjusting the calcination temperature of WO_x–ZrO_2. *Mater. Chem. Phys.* **2013**, *138*, 399–404. [CrossRef]
42. Hong, W.J.; Ueda, M.; Iwamoto, S.; Hosokawa, S.; Wada, K.; Kanai, H.; Deguchi, H.; Inoue, M.J. Effect of Fe content on physical properties of BaO–CeO_x –FeO_y catalysts for direct NO decomposition. *J. Catal.* **2011**, *106*, 142–148. [CrossRef]
43. Liu, F.; He, H.; Zhang, C.; Feng, Z.; Zheng, L.; Xie, Y.; Hu, T.J. Selective catalytic reduction of NO with NH_3 over iron titanate catalyst: Catalytic performance and characterization. *Appl. Catal. B Environ.* **2010**, *96*, 408–420. [CrossRef]
44. Zhang, X.; Yang, Y.; Lv, X.; Wang, Y.; Cui, L. Effects of Preparation Method on the Structure and Catalytic Activity of Ag-Fe_2O_3 Catalysts Derived from MOFs. *Catalysts* **2017**, *7*, 382. [CrossRef]
45. Parry, E.P. An infrared study of pyridine adsorbed on acidic solids. Characterization of surface acidity. *J. Catal.* **1963**, *2*, 371–379. [CrossRef]

46. Emeis, C.A. Determination of Integrated Molar Extinction Coefficients for Infrared Absorption Bands of Pyridine Adsorbed on Solid Acid Catalysts. *J. Catal.* **1993**, *141*, 347–354. [CrossRef]
47. Xin, Z.; Tao, L.; Rong, L.; Bai, T.; Zhang, G.J.I.; Research, E.C. Properties and Reactivity of Fe–P–O Catalysts Prepared by Different Methods for Benzylation of Benzene. *Ind. Eng. Chem. Res.* **2012**, *51*, 3541–3549. [CrossRef]
48. Shi, A.; Wang, X.; Yu, T.; Shen, M.J. The effect of zirconia additive on the activity and structure stability of V_2O_5/WO_3-TiO_2 ammonia SCR catalysts. *Appl. Catal. B Environ.* **2011**, *106*, 359–369. [CrossRef]
49. Wu, Z.; Jiang, B.; Liu, Y.; Zhao, W.; Guan, B. Experimental study on a low-temperature SCR catalyst based on MnO_x/TiO_2 prepared by sol-gel method. *J. Hazard. Mater.* **2007**, *145*, 488–494. [CrossRef]
50. Shen, B.; Liu, T.; Zhao, N.; Yang, X.; Deng, L. Iron-doped Mn-Ce/TiO2 catalyst for low temperature selective catalytic reduction of NO with NH3. *J. Environ. Sci.* **2010**, *22*, 1447–1454. [CrossRef]
51. Kwon, D.W.; Nam, K.B.; Hong, S.C. Influence of tungsten on the activity of a Mn/Ce/W/Ti catalyst for the selective catalytic reduction of NO with NH3 at low temperatures. *Appl. Catal. A Gen.* **2015**, *497*, 160–166. [CrossRef]
52. Fang, D.; Xie, J.L.; Hu, H.; Zhang, Z.; He, F.; Zheng, Y.; Zhang, Q. Effects of precursors and preparation methods on the potassium deactivation of MnO_x/TiO_2 catalysts for NO removal. *Fuel Process. Technol.* **2015**, *134*, 465–472. [CrossRef]
53. Li, B.; Wang, H.; Ding, F.C.; Li, C.Q.; Song, Y.J.; Ke, M.; Ren, C.T. Effects of Preparation Methods on the Catalytic Performance of Selective Catalytic Reduction of NO with CH_4 over Co-MOR Catalysts. *Acta Phys.-Chim. Sin.* **2013**, *29*, 1289–1296. [CrossRef]
54. He, L.F.; Liu, J.D.; Huang, W.; Li, Z. Effect of Preparation Methods on Performance of Mn-Ce/ZSM-5 Catalyst for Low-temperature Selective Catalytic Reduction of NO. *Chem. J. Chin. Univ.* **2012**, *33*, 2532–2536. (In Chinese) [CrossRef]
55. Liu, J.; Li, G.Q.; Zhang, Y.F.; Liu, X.Q.; Wang, Y.; Li, Y. Novel Ce-W-Sb mixed oxide catalyst for selective catalytic reduction of NOx with NH_3. *Appl. Surf. Sci.* **2017**, *401*, 7–16. [CrossRef]
56. Catlow, C.R.A. Atomistic mechanisms of ionic transport in fast-ion conductors. *J. Chem. Soc.-Faraday Tran.* **1990**, *86*, 1167–1176. [CrossRef]
57. Liu, F.; He, H.; Ding, Y.; Zhang, C. Effect of manganese substitution on the structure and activity of iron titanate catalyst for the selective catalytic reduction of NO with NH_3. *Appl. Catal. B-Environ.* **2009**, *93*, 194–204. [CrossRef]
58. Wang, H.; Qu, Z.; Dong, S.; Tang, C. Mechanism study of FeW mixed oxides to the selective catalytic reduction of NOx with NH3: in situ DRIFTS and MS. *Catal. Today* **2018**, *307*, 35–40. [CrossRef]
59. Devaiah, D.; Reddy, L.H.; Park, S.-E.; Reddy, B.M. Ceria–zirconia mixed oxides: Synthetic methods and applications. *Catal. Rev.* **2018**, *60*, 177–277. [CrossRef]
60. Xu, H.; Li, Y.; Xu, B.; Cao, Y.; Feng, X.; Sun, M.; Gong, M.; Chen, Y. Effectively promote catalytic performance by adjusting W/Fe molar ratio of $FeW_x/Ce_{0.68}Zr_{0.32}O_2$ monolithic catalyst for NH_3-SCR. *J. Ind. Eng. Chem.* **2016**, *36*, 334–345. [CrossRef]
61. Qi, G.S.; Yang, R.T. Performance and kinetics study for low-temperature SCR of NO with NH_3 over MnO_x-CeO_2 catalyst. *J. Catal.* **2003**, *217*, 434–441. [CrossRef]
62. Qi, G.S.; Yang, R.T.; Chang, R. MnO_x-CeO_2 mixed oxides prepared by co-precipitation for selective catalytic reduction of NO with NH_3 at low temperatures. *Appl. Catal. B Environ.* **2004**, *51*, 93–106. [CrossRef]